In-depth structural analysis of swift heavy ion irradiation in KY(WO$_4$)$_2$ for the fabrication of planar optical waveguides

RAIMOND FRENTROP,[1,6] ⬤ ILIA SUBBOTIN,[2] FRANS SEGERINK,[1] RICO KEIM,[1] VICTORIA TORMO-MARQUEZ,[3] JOSÉ OLIVARES,[3,4] KIRILL SHCHERBACHEV,[5] SERGEY YAKUNIN,[2] IGOR MAKHOTKIN,[1] AND SONIA M. GARCIA-BLANCO[1,7] ⬤

[1]*MESA+ Institute for Nanotechnology, University of Twente, P.O. Box 217, 7500 AE Enschede, The Netherlands*
[2]*National Research Center "Kurchatov Institute", 1, Akademika Kurchatova pl., Moscow, 123182, Russia*
[3]*Centro de Microanálisis de Materiales (CMAM), Universidad Autónoma de Madrid (UAM), 28049 Madrid, Spain*
[4]*Instituto de Óptica, Consejo Superior de Investigaciones Científicas, (IO, CSIC), C/Serrano 121, 28006 Madrid, Spain*
[5]*National University of Science and Technology MISIS, 4, Leninsky avenue, Moscow, 119049, Russia*
[6]*r.n.frentrop@utwente.nl*
[7]*s.m.garciablanco@utwente.nl*

Abstract: Rare-earth ion doped KY(WO$_4$)$_2$ is a well-known active laser crystal, due to its excellent gain characteristics and its relatively high nonlinear refractive index. As these properties are of great benefit to applications in integrated photonics, a study has been done into the fabrication of high refractive index contrast slab waveguides in KY(WO$_4$)$_2$ as a first step towards the fabrication of channel waveguides. When properly choosing the fluence and annealing parameters, ion irradiation with 12 MeV carbon ions produces a step-like damage profile. Confocal Raman microscopy, X-ray diffraction and transmission electron microscopy are used in this work to study the structural damage induced by ion irradiation. The characterization indicates damage to the crystal structure due to the ion irradiation that increases as a function of both depth and ion fluence till the threshold for amorphization is achieved. Successive annealing steps of the irradiated crystals at different temperatures show partial repair of the crystalline structure when the irradiation did not fully amorphize the material. When the threshold of amorphization was reached, annealing further increases the damage induced by the irradiation. By tuning the irradiation fluence, a high-refractive index contrast slab waveguide in KY(WO$_4$)$_2$ produced by ion irradiation was demonstrated.

1. Introduction

Integrated on-chip amplifiers and lasers [1,2] find many applications in various fields, including telecommunications [3], datacom [4], biosensing [5,6] and LIDAR [7] amongst others. Potassium double tungstates (i.e., KY(WO$_4$)$_2$, KGd(WO$_4$)$_2$, in short KRE(WO$_4$)$_2$) - used for decades as active materials for high-power ultra-short pulsed lasers [8–10], thin-disk lasers [11,12] and Raman lasers [13–15] - have been recently demonstrated to deliver high gain per unit length in low-contrast waveguide amplifiers [16] and lasers [17–19], thanks to their high rare-earth ion solubility (together with a large interionic distance), high absorption and emission cross-sections when doped with rare-earth ions, and high achievable pump intensity in waveguide configuration. Even higher efficiency could be obtained by the fabrication of high-refractive index contrast waveguides in KY(WO$_4$)$_2$. Heterogeneous integration (e.g. bonding onto a SiO$_2$ substrate

followed by thinning and lapping to the desired thickness) is the method primarily proposed for the realization of such high-refractive index contrast waveguides [20]. Control of the final layer thickness is the biggest challenge in this method and strategies such as a polishing stop have been proposed [21]. In this study, swift-ion irradiation is proposed as an alternative method to fabricate thin, high-refractive index contrast, low-loss slab optical waveguides in bulk potassium double tungstate crystals. Preliminary studies on waveguide formation in $KGd(WO_4)_2$ by light [22] and heavy ion irradiation [23,24] have already demonstrated the potential of this technique. These studies have shown a higher refractive index change induced by swift heavy ion irradiation in $KGd(WO_4)_2$ (~0.13 [23]) compared to light ion irradiation (He^+: ~0.01 [25], H^+: ~0.003 [22]), allowing for the fabrication of high-contrast waveguides in $KRE(WO_4)_2$ crystals. More recently, optical characterization has shown that low optical losses of <1.5 dB/cm at 1550 nm can be achieved in slab waveguides using carbon ion irradiation [26]. To design low-loss, high-refractive index contrast optical waveguides in $KY(WO_4)_2$ with the desired cross-sectional characteristics, an understanding of the dependence of the material structural changes on the parameters of the ion irradiation process is necessary.

In this paper, the structural changes induced in $KY(WO_4)_2$ by 12 MeV carbon ion irradiation, both as function of irradiation fluence and annealing temperature, have been investigated using confocal Raman microscopy, high-resolution X-ray diffraction (HRXRD) and transmission electron microscopy (TEM). A direct relation was observed between the structural and vibrational change in the $KY(WO_4)_2$ crystal and the ion fluence. Further changes as a function of post-irradiation annealing temperature show two different damage regimes, namely above and below the amorphization threshold. Below this threshold, partial repair of the irradiation-induced damage can be observed by the recovery of the $KY(WO_4)_2$ Raman spectrum and the TEM diffractogram. Above the amorphization threshold, an increase in annealing temperature leads to consolidation of the irradiation damage. Finally, micro-reflectivity measurements were carried out to study the refractive index change as a function of depth and ion fluence. The results of these measurements indicate that this method is very promising for the fabrication of high-refractive index contrast slab waveguides.

2. Experimental methods

The $KY(WO_4)_2$ crystals [27] of dimensions $10x10x1\ mm^3$ (surface in the *a-c* plane) used in this study were purchased from Altechna (LT), and subsequently cut in half along the *c*-axis. For the irradiations, the $10x5x1\ mm^3$ samples were attached to a sample holder using copper tape to avoid charging. Irradiation of the samples was performed in the 5 MV electrostatic tandem accelerator [28] from the Centro de Microanálisis de Materiales de Madrid, with the sample surface tilted at a 5°angle to avoid channelling. The ion beam area was set to $3x3\ cm^2$ to ensure an even ion fluence over the sample, and the ion current was kept below 1 μA to avoid heating of the samples above 60°C during irradiation.

Damage in the material originates from two mechanisms [29]. At high ion energy the majority of the damage is caused by inelastic ion-electron interactions and subsequent thermal spiking. The profile of this damage follows the Lindhard-Scharf-Schiott theory [30]. At lower ion energy, elastic nuclear collisions between the ion and the atoms in the material become the main cause of damage. The dominant damage type, damage profile and extent depend on several parameters including the ion type, ion energy and ion charge state, and the target material.

Increasing the irradiation fluence over a certain value causes complete amorphization of the material. The minimum fluence at which full amorphization happens is called the amorphization threshold. Previous irradiation research on $KGd(WO_4)_2$ indicated that carbon ions induce the most step-like damage profile in $KRE(WO_4)_2$, because they are just heavy enough (A>12) and of high enough energy (E>4 MeV) for the electronic energy loss to dominate over the nuclear energy loss [24]. Carbon ion irradiation forms a damage barrier around the maximum of the electronic

stopping force, while the surface of the crystal remains relatively undamaged [23], therefore potentially producing well-confined low-loss slab waveguides. The depth of the maximum electronic damage in $KY(WO_4)_2$ was chosen at ~4 μm to ease the structural characterization. The corresponding carbon ion energy was calculated using SRIM-2013 [31] to be 12 MeV (Fig. 1(a)). Figure 1(b) shows the $KY(WO_4)_2$ crystal indicating the location of both the electronic and nuclear damage regions and the different crystalline axes.
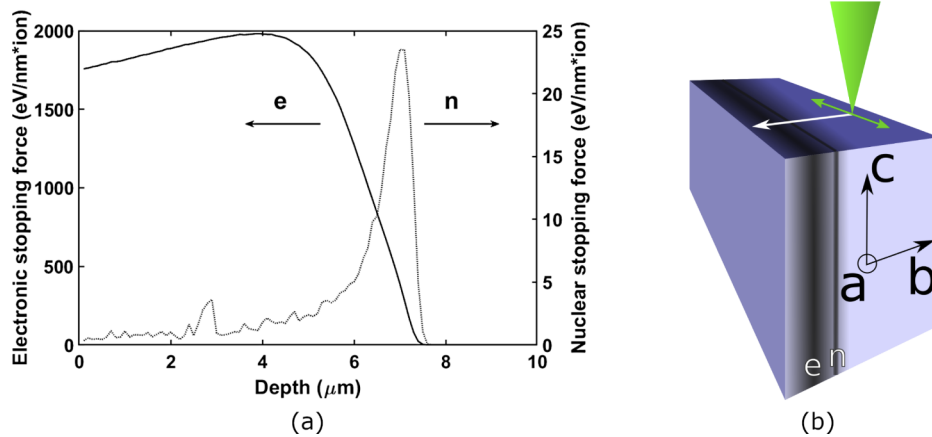

Fig. 1. (a) Electronic ('e', solid line) and nuclear ('n', dotted line) stopping force curves for a single ion, calculated by SRIM-2013 for irradiation of $KY(WO_4)_2$ with 12 MeV carbon ions. The arrows indicate the y-axis for both lines. (b) Schematic indication of the scanning method used for the confocal Raman microscope line scans. The white arrow indicates the scanning direction, the green arrow indicates the direction of oscillation of the incident electric field, and the green cone depicts the focused excitation light. Scanning was started in the bulk (undamaged) crystal because correct focusing was performed using the known Raman signal of the bulk $KY(WO_4)_2$.

After irradiation, the a-b end-facets of the samples were polished using a Logitech MP5 (UK) polishing instrument with a 40 nm SiO_2 suspension. To avoid rounding effects, the samples were surrounded by hard polishing wax, which required the samples to be heated to 100°C both before and after polishing. Subsequently, the samples were cleaned with trichloroethylene, acetone and isopropanol in an ultrasound bath to remove all traces of the copper tape adhesive, polishing wax and polishing suspension.

Raman characterization of the irradiated crystals was performed using a WiTec alpha300R/S/A confocal Raman microscope. A CW laser diode (λ=532 nm) with a measured power on the sample of 45 mW was used as excitation source. Using a 100x 0.9NA objective, a lateral resolution of ~200 nm and a focal depth of ~700 nm were achieved. Raman spectra were recorded with the excitation and collection beams propagating perpendicular to the *a-b* end-facet, with the excitation electric field polarized along the *a*-axis, in steps of 100 nm along the *b*-axis (Fig. 1(b)). Collection of the Raman spectra was performed without analysing polarizer, using an integration time of 0.5 s, and 2 accumulations were averaged to reduce shot noise. The static spectral background was measured with the spectrometer shutter closed, and subtracted from all measurements. All spectra were normalized to the intensity of the 906 cm^{-1} $KY(WO_4)_2$ Raman peak in the unirradiated region of the sample. The $KY(WO_4)_2$ samples under investigation were irradiated with 12 MeV carbon ions at fluences of $4\cdot10^{13}$ ions/cm^2, $1\cdot10^{14}$ ions/cm^2, $2.7\cdot10^{14}$ ions/cm^2, $4 \cdot 10^{14}$ ions/cm^2 and $8\cdot10^{14}$ ions/cm^2. The damage effects induced by these ion fluences were studied before and after annealing steps at different temperatures. Analysis of the Raman spectra permits obtaining qualitative information on the structural modifications

induced by the irradiation, based on the analysis of the vibrational frequencies and peak intensities. Several factors, including excitation polarization, quality of the polished surface and focal spot volume, have influence on the measurements, making the extraction of quantitative data difficult.

HRXRD curves were measured at the National Research Center "Kurchatov institute" in a Bragg reflection geometry. A Rigaku SmartLab (Japan) X-ray diffractometer was used with a rotating anode, in a high-resolution scheme with a parallel beam mirror, a 2-bounce Ge(022) monochromator, and collimating slits. CuKα1 radiation (λ=1.54056 Å) was used. The distribution of intensity in the vicinity of the (040) reciprocal lattice point was analyzed. To separate coherent and non-coherent (diffuse) contributions to the diffraction, the intensity was analyzed along the sections perpendicular to the diffraction vector (qx-scans) located at different distances from the (040) reciprocal lattice point. The model of the structure is described by both strain and static Debye-Waller factor profiles (DWF). To take partial amorphization of an implanted layer into account, the Debye-Waller factor, given by $\exp(-L_H)$, was introduced into a description of the damaged layer model. The value of L_H depends linearly on the mean square displacements $\langle u^2 \rangle$ of the atoms from their sites in the crystal lattice:

$$L_H = 8 \left(\pi \frac{\sin \theta_B}{\lambda} \right)^2 \langle u^2 \rangle \tag{1}$$

where θ_B is the Bragg angle and λ is the wavelength of the incident X-rays. The Fourier components of the polarizability in a distorted crystal can be rewritten as [32]

$$\chi_h^* = \chi_h e^{-L_H} \tag{2}$$

where χ_h is the direct beam intensity and χ_h^* is the intensity of the diffracted wave. Since $0<\text{DWF}=\exp(-L_H)\leq1$, the magnitude of the DWF, which is related to the amount of damage in the layer (i.e., in the form of lattice deformation and defect density), can be extracted from the decrease of the measured diffracted wave amplitude $\left| \chi_h^* \right|$. The profiles, defined by several base points and a piecewise cubic Hermite interpolating polynomial function (PCHIP) [33], can be determined from the shape of the diffraction curve. As an initial approximation, the thickness of the damaged layer was determined by the intensity of the main Bragg peak, which depends on the direct beam intensity normalized by the relative intensity and the absorption in the deformed layer. Simulation of the curves of diffraction reflection was performed in the framework of the dynamical theory of X ray diffraction, using formalism suggested by Wie et al. [34]. To reconstruct the profiles, we used an auto-fitting procedure similar to the one used by Chtcherbatchev et al. [35]. HRXRD measurements were performed on the samples irradiated with 1•10^{14} ions/cm^2 and 4•10^{14} ions/cm^2 carbon ions before and after annealing at 350°C for 30 minutes. Analysis of the HRXRD measurements allows for a quantitative analysis of the strain and crystalline damage in the material, due to the fact that HRXRD can directly measure changes in the lattice parameters as well as defect formation.

Transmission electron microscopy images and diffractograms were taken using a Philips CM300ST-FEG 300 kV TEM. Samples were prepared using a focused ion beam process in a FEI Nova600 NanoLab Dualbeam-SEM/FIB system and mounted on an Omniprobe molybdenum 3-post lift-out grid [36]. A thin platinum layer was deposited on top of the KY(WO$_4$)$_2$ to provide sufficient conduction. Due to the FIB preparation process, both facets of the sample have a thin amorphous surface layer. The thickness of this layer is reduced to about 3-5 nm in the last stages of the preparation process using a 5 kV and 2 kV cleaning step. The final thickness of the prepared KY(WO$_4$)$_2$ slab is approximately 60-80 nm. The TEM system uses a Gatan Ultrascan1000 CCD camera, and has a resolution of approximately 0.1 nm.

3.   Results

3.1.   Structural damage as function of ion fluence

The Raman spectra of two of the investigated fluences as a function of depth into the material, (i.e., $1 \cdot 10^{14}$ ions/cm^2 and $4 \cdot 10^{14}$ ions/cm^2) are shown in Fig. 2. These fluences reflect the situations for which the amorphization threshold is not reached ($1 \cdot 10^{14}$ ions/cm^2, Fig. 2(a)), and for which the amorphization threshold is reached in a region around the maximum of the electronic stopping force ($4 \cdot 10^{14}$ ions/cm^2, Fig. 2(b-c)). Damage to the crystalline structure is evidenced by both a decrease in peak intensity and an increase in peak FWHM throughout the KY(WO$_4$)$_2$ spectrum for both fluences. The highest structural damage occurs at the maximum of the electronic ($\sim$4 μm) and nuclear ($\sim$7 μm) stopping forces, where all Raman peaks show the same relative peak intensity reduction indicating amorphization. Regions of the samples damaged below the amorphization threshold [29] partially retain the Raman peaks characteristic for KY(WO$_4$)$_2$, with a new, broad-band peak appearing at 953 cm^{-1}, indicating amorphization of the material. Above the amorphization threshold no KY(WO$_4$)$_2$ Raman spectrum can be observed but only the new broad-band amorphous spectrum with maximum at 953 cm^{-1}.
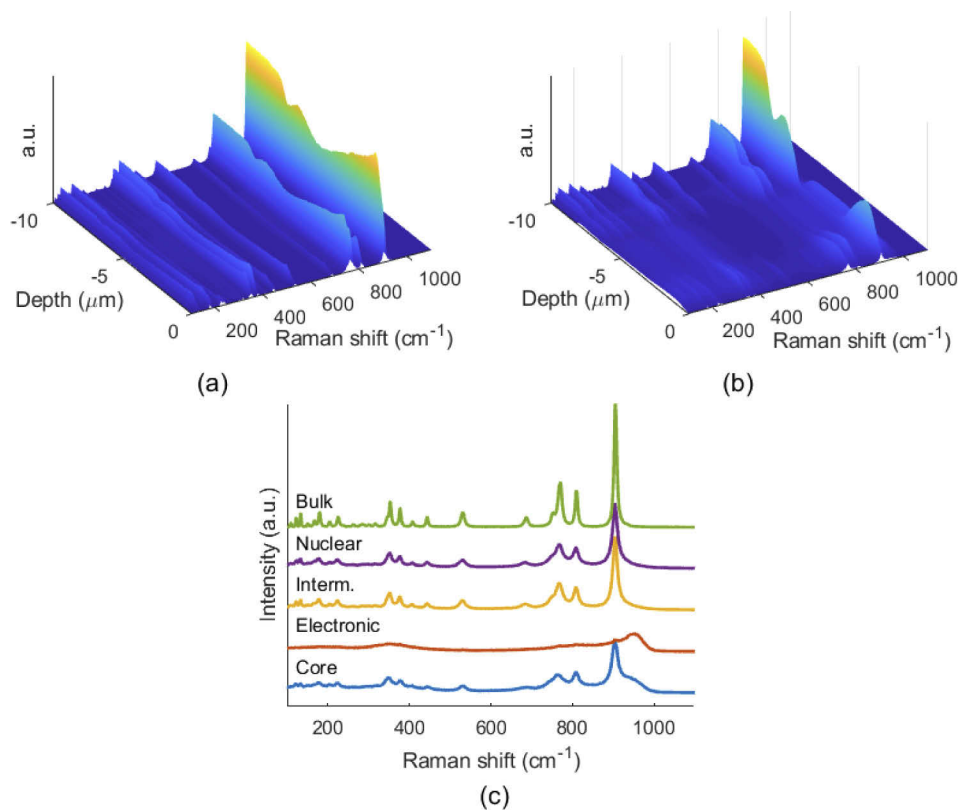

Fig. 2. 3D plot of Raman line scans of KY(WO$_4$)$_2$ crystals after 12 MeV carbon irradiation at fluences of (a) $1 \cdot 10^{14}$ ions/cm^2 and (b) $4 \cdot 10^{14}$ ions/cm^2, accompanied by (c) the Raman spectra at several depths into the material for the sample irradiated with $4 \cdot 10^{14}$ ions/cm^2; close to the surface (core), at the locations of maximum electronic damage (electronic), between the electronic and nuclear maxima (intermediate), at the nuclear barrier (nuclear) and far away from the irradiation damage (bulk).

There is a direct relation between the carbon ion fluence and the damage to the crystalline structure indicated by the evolution of the 906 cm^{-1} vibrational KY(WO$_4$)$_2$ peak intensity and position as function of depth (Fig. 3). The Raman change saturates to a full amorphous spectrum in at least part of the crystal for fluences $\geq$2.7 • 10^{14} ions/cm^2. In these regions no data is shown because the 906 cm^{-1} peak is buried within the new broadband peak with maximum at 953 cm^{-1}. As the ion fluence increases, the amorphization induced by the electronic interactions (i.e., electronic barrier) widens, extending towards the sample surface and deeper into the material, while the nuclear interactions (i.e., nuclear barrier) shifts deeper into the substrate. The vibrational frequency of the 906 cm^{-1} is lowered as the fluence increases, which is visible in both the electronic and nuclear barriers (i.e., in the electronic barrier amorphization is reached and, therefore, the 906 cm^{-1} disappears). Using the crystallinity information provided by Raman microscopy for all fluences, the amorphization threshold for carbon ions in KY(WO$_4$)$_2$ can be approximated. The material starts amorphizing at the maximum of the electronic damage for ion fluences of >2.7•10^{14} ions/cm^2. The amorphization threshold in displacements per atom (dpa) can be calculated as the displacements per ion per unit length (displacements/ion*nm) at the maximum stopping force per ion multiplied by the fluence (ions/cm^2) that just induces amorphization, divided by the atomic density (atoms/cm^3) of KY(WO$_4$)$_2$. Using a material density of ρ = 6.61 g/cm^3, molar weight of KY(WO$_4$)$_2$ of 623.68 g/mol, a fluence of 2.7•10^{14} ions/cm^2, and 0.0515 displacements per ion per nm (calculated by SRIM-2013), the amorphization threshold equals

$$\frac{5.2 \cdot 10^5 \left[\frac{displacements}{ion*cm}\right] \times 2.7 \cdot 10^{14} \left[\frac{ion}{cm^2}\right]}{7.66 \cdot 10^{22} \left[\frac{atom}{cm^3}\right]} = 1.8 \cdot 10^{-3}\ dpa \tag{3}$$
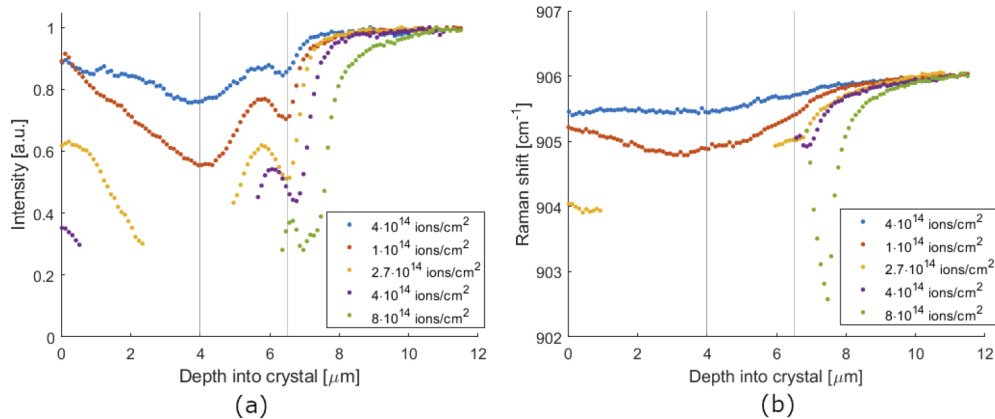

Fig. 3. Evolution of the 906 cm^{-1} KY(WO$_4$)$_2$ Raman peak intensity (normalized to bulk intensity) and exact Raman shift as function of depth of different irradiated samples with various fluences, prior to annealing. The vertical lines indicate the SRIM-2013 calculated depth of the maximum electronic and nuclear stopping forces. The peak wavenumber and intensity were determined by fitting of the spectral data with a Lorentzian profile.

The HRXRD measurements allow for a quantitative analysis of the strain and crystalline fraction in different regions along the irradiation trajectory. These regions are indicated in Fig. 4. Four regions can be identified: the surface region (A), the region of defect accumulation (B), the relaxation region (C) and the bulk crystal (D). In the surface region, a higher deformation is measured in the first <0.5 μm indicating strain at the surface. The defect accumulation region (B) is associated with the creation of damage due to inelastic interactions between the ion and target

material (i.e., electronic damage), and can be identified by a decreasing DW factor due to damage creation, and an increasing deformation caused by damage-induced strain. After the maximum of the irradiation damage, the crystal strain relaxes (C) and the amount of deformation and the DW factor return to bulk values. The period of the oscillations on the HRXRD experimental data (see Fig. 4) determines the thickness layer between maxima of the deformation and the maximum ion depth. The relaxation region has a lower DW factor due to the implantation of the carbon
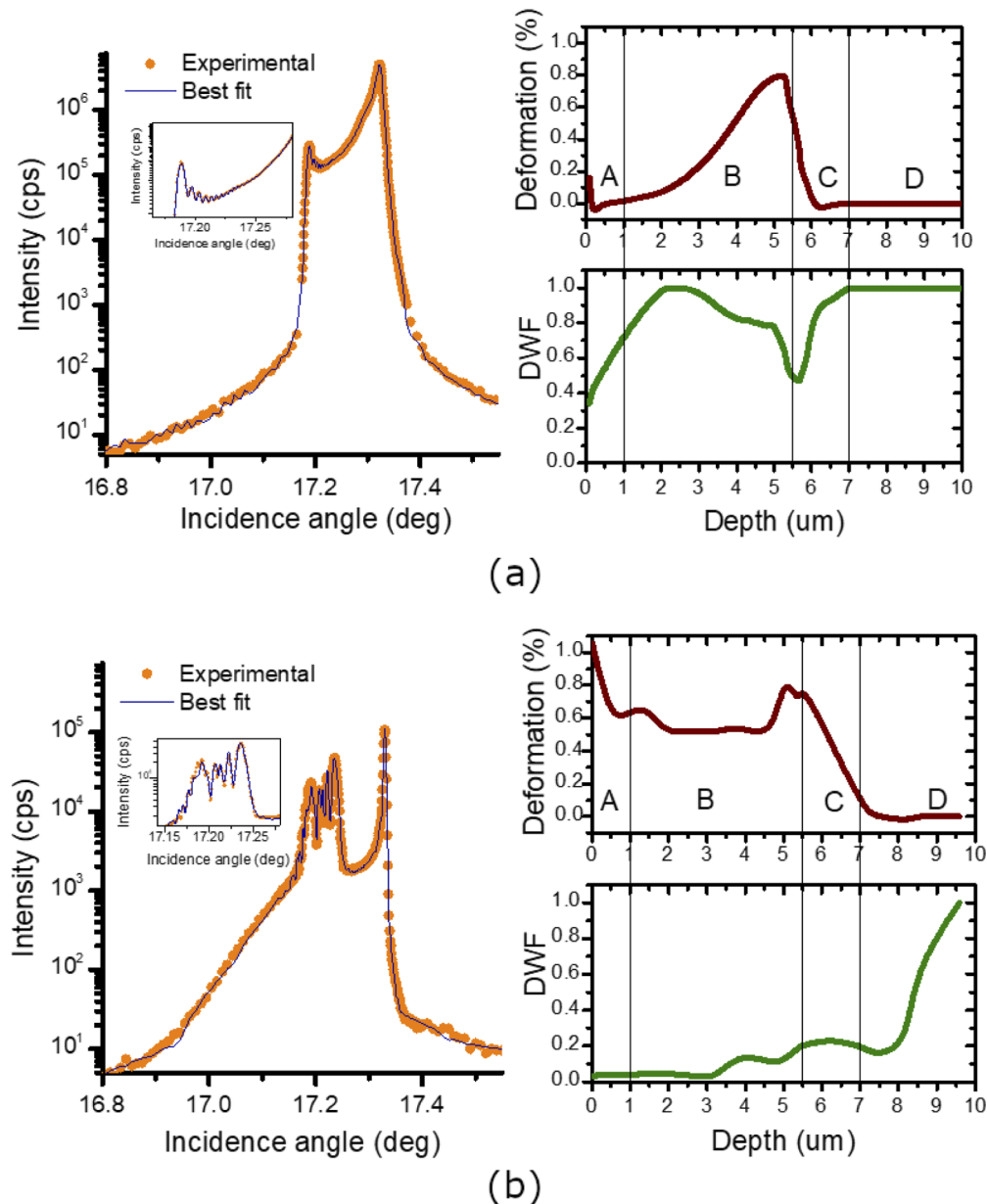

Fig. 4. The HRXRD scan data with fit, and the lattice parameter deviation along the *b*-axis and the Debye-Waller factor (crystallinity factor) as function of depth into the crystal, reconstructed from the HRXRD data for 12 MeV carbon irradiated $KY(WO_4)_2$ at fluences of (a) $1 \cdot 10^{14}$ ions/cm^2 and (b) $4 \cdot 10^{14}$ ions/cm^2.

ions, which causes point defects. For an irradiation fluence below the amorphization threshold (Fig. 4(a)), the DW factor is lowered and indicates that half of the material is still crystalline (i.e., DWF>0.5). Most of the crystal structure damage is located at a depth of 5-6 µm, but the strain caused by this damage extends towards the surface as well as deeper into the material. When the irradiation fluence is increased (Fig. 4(b)), the DW factor indicates that the damage extends towards the surface as well as further into the material, and the relaxation region (C) is much wider compared to the lower fluence. Both effects were already observed in the Raman scans in Fig. 3. The presence of a significant amount of deformation together with a very low DW factor indicates the conversion of the structure of the material from monocrystalline to polycrystalline with small-angle boundaries. Both the low and high fluence irradiated crystals indicate the presence of strain at or very close to the surface. The origin of this strain is unclear but could be caused by the presence of ion impact damage.

TEM images and diffractograms (Fig. 5) were taken to help in the interpretation of the HRXRD and Raman results. The surface region (Fig. 5(a)), damage accumulation region (Fig. 5(b)) and maximum damage region (Fig. 5(c)) can be identified and they match the location of the regions A, B and C in the HRXRD results, respectively. The diffractograms, as well as the TEM images, clearly indicate a monoclinic crystalline structure in the surface region (Fig. 5(a)), although some amorphization is already present. For an increasing amount of crystal imperfections (Fig. 5(b)) the crystal first becomes polycrystalline with large grains, and further damage decreases the grain size to an almost amorphous state at the maximum of the electronic damage (Fig. 5(c)). The polycrystallinity could explain the HRXRD results for higher ion fluence; the DW factor approaches zero due to the polycrystalline nature of the material, while the deformation within these polycrystalline islands can still be measured. At the maximum of the electronic damage (Fig. 5(c)), the material has been completely converted to an amorphous structure.
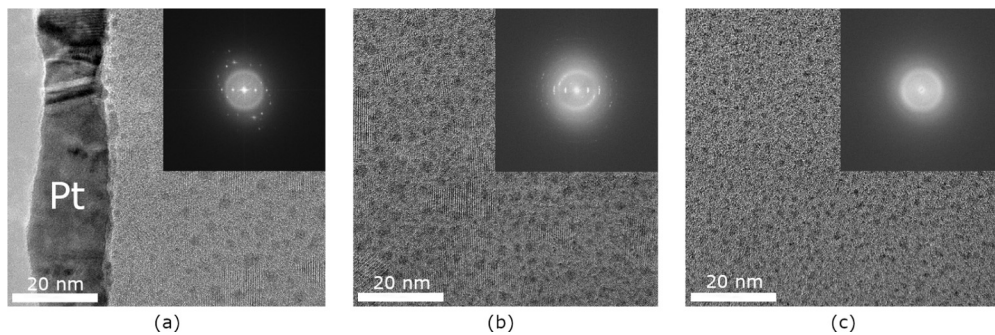

Fig. 5. TEM images of the structure of an as-irradiated sample (fluence $2.7 \cdot 10^{14}$ ions/cm^2) at three different depths along the irradiation path: (a) the surface, (b) just outside the amorphous barrier (depth of 2.5 µm), and (c) inside the amorphous barrier. Damage appears in the form of black dots, changes in crystal orientation and disappearance of the crystalline structure. The last two effects are also present in the diffractogram as smeared lines and a raised background, respectively.

3.2. Structural changes due to annealing

For waveguide fabrication, an annealing step is essential to lower scattering losses in the core region. The 12 MeV carbon irradiated KY(WO$_4$)$_2$ samples were consecutively annealed at temperatures increasing from 200°C to 350°C in steps of 50°C. The annealing was performed by ramping to the target temperature with a slope of 2°C/min from room temperature, after which it was kept stable for 30 minutes in a temperature-controlled oven. Afterwards, the samples were left to cool down in the oven for several hours. Raman line scans were recorded at room

temperature after each annealing step. The intensity of the 906 cm^{-1} Raman peak normalized to the intensity in the bulk clearly shows the effects of annealing in the structure of the irradiated samples (Fig. 6). In regions with below-threshold damage (Fig. 6(a)), the Raman spectrum partially restores toward the undamaged KY(WO$_4$)$_2$ spectrum (ie., increase of the intensity of the 906 cm^{-1} peak). For crystals irradiated above the amorphization threshold (Fig. 6(b-c)) the scans show that there is only a slight change in the Raman profile, both in the surface region (0-2 μm) as well as in the nuclear barrier, after annealing at 350°C. Figure 6(c) shows the intensity of the 953 cm^{-1} peak, which indicates amorphization. The intensity of this peak increases as the annealing temperature increases, implying consolidation of the damage in the electronic damage region that was irradiated above the amorphization threshold. A decrease in Raman intensity close to the surface is observed in most of the measurements, in agreement with the increase in deformation at the surface observed in the HRXRD analysis. TEM images and diffractograms (Fig. 7) also indicate partial repair of the crystal structure, with the KY(WO$_4$)$_2$ diffraction pattern reappearing in the amorphized regions.
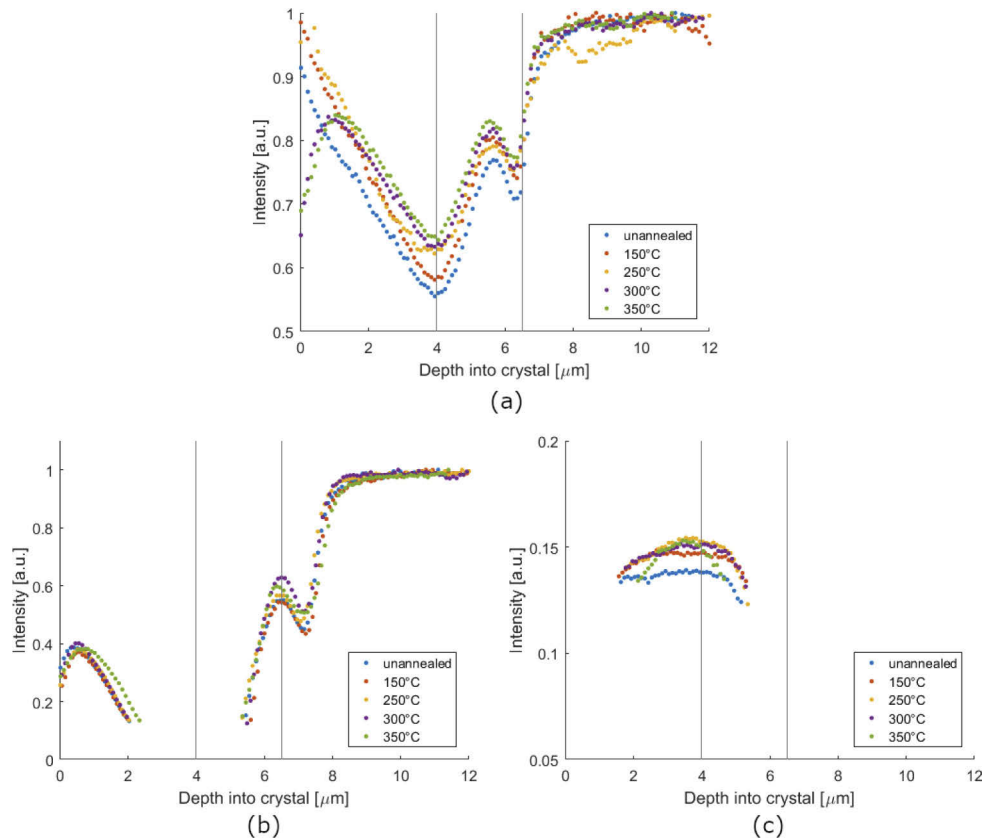

Fig. 6. Raman analysis of a (a) 1•10^{14} ions/cm^2 and (b-c) 4•10^{14} ions/cm^2 irradiated crystal, after annealing at several temperatures, showing the peak intensity of the 906 cm^{-1} KY(WO$_4$)$_2$ peak (a-b) and 953 cm^{-1} amorphous peak (c) after least-squares fitting to a Lorentzian profile, as function of depth into the crystal. The peak intensity is normalized to the peak height in the unirradiated Raman signal.

An HRXRD scan of the above-threshold sample was made to gain more insights on the effects of annealing on the crystalline quality (Fig. 8). Damage as well as strain at the surface increase (with a maximum deformation of ~2%, compared to ~1.2% for Fig. 4(b)), which is in agreement
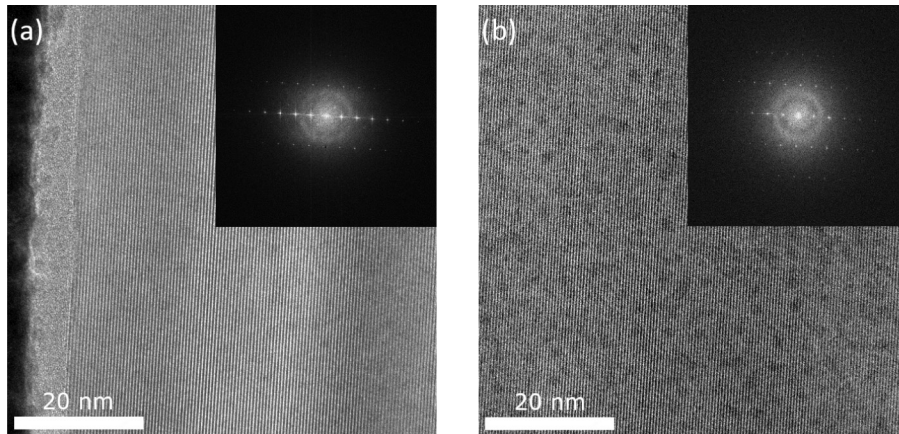
Fig. 7. TEM images of annealing at 350°C of a $2.7 \cdot 10^{14}$ ions/cm^2 irradiated sample, at (a) the surface, and (b) close to the amorphous barrier (depth of 2.5 μm). In both cases most of the damage is repaired, but small displacements and black spots are still visible, and from the diffractogram its clear an amorphous fraction is still present.

with the suggestion of surface damage from the Raman measurements (Fig. 6). Additionally the DW factor increases significantly while the average deformation has lowered to ~0.2%. The nuclear damage region moves slightly deeper into the crystal, most likely caused by the migration of the implanted carbon ions. The maximum deformation in this region is lowered from 0.78% before annealing to 0.6% because part of the carbon ions settle into the crystalline structure, but clearly vacancies still remain.
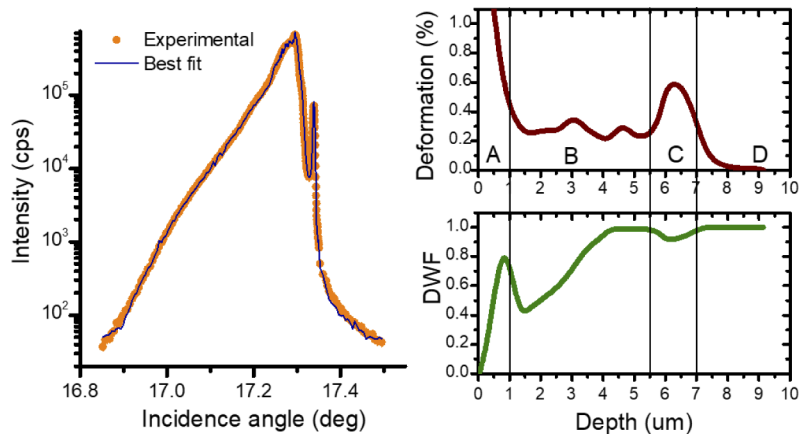

Fig. 8. HRXRD scan data with fit, lattice parameter deviation along the b axis and Debye-Waller factor (crystallinity factor) as function of depth into the crystal, reconstructed from the HRXRD data of KY(WO$_4$)$_2$ irradiated at a fluence of $4 \cdot 10^{14}$ ions/cm^2 after annealing at 350°C.

3.3. *Optical characterization*

As the goal of the research is the fabrication of high index contrast optical waveguides in KY(WO$_4$)$_2$, the refractive index profile as function of depth and ion fluence was measured using a micro-reflectivity setup [37] (Fig. 9), with the incident electric field polarized along the *a*-axis.

All measurements were performed on crystals directly after irradiation without a first annealing step. The reason for this is that for the highest fluences (>4•10^{14} ions/cm^2) annealing at 350°C created cracks in the crystal due to recrystallization in the barrier, which prohibited the refractive index measurement. However, it is expected that no significant changes in the refractive index profile will occur due to annealing as the Raman profiles (Fig. 6) indicate limited recovery of the crystalline structure, and the resolution of the micro-reflectivity measurement (approx. 0.02 RIU) is smaller than the expected change in refractive index. A reduction of the refractive index is observed due to the amorphization of the material, which begins at the maximum of the electronic interactions and extends towards the crystal surface and deeper into the material as the fluence increases. A maximum refractive index change of ~0.2 can be achieved above the amorphization threshold. The refractive index at the crystal surface stays close to the refractive index of the unirradiated KY(WO$_4$)$_2$ (n=2.04 at 1550 nm) due to the lower damage in this region. By controlling the irradiation fluence and annealing temperature, a step-like refractive index profile can be achieved. The stress observed by both XRD and Raman measurements between the crystalline and amorphous layers was expected to lead to polarization dependent changes in the refractive index profile [23]. However, the limited spatial and refractive index resolution of our micro-reflectivity profile did not allow us to observe such effects in our measurements.
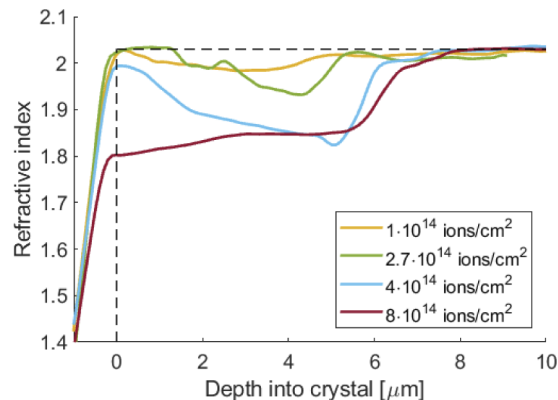

Fig. 9. Refractive index of the 12 MeV carbon ion irradiated KY(WO$_4$)$_2$, measured using a micro-reflectivity type setup with a wavelength of 532 nm and incident electric field polarized along the *a*-axis. The bulk refractive index of KY(WO$_4$)$_2$ at this wavelength is ~2.04. The vertical and horizontal dashed lines indicate the crystal surface and bulk refractive index, respectively.

A slab waveguide was fabricated using a fluence of 2.7•10^{14} ions/cm^2 accelerated at an energy of 9 MeV [26]. This energy was chosen to obtain a single mode waveguide after the fabrication of strip waveguides. Figure 10(a) shows the propagation of 1550 nm light coupled with a prism coupler into the fundamental mode of the slab waveguide. Analysis of the exponential decay of the light strike shows propagation losses of ~1.5 dB/cm. Figure 10(b) shows the reflected intensity from a coupling prism (i.e. in an Metricon 2010/M setup), clearly showing the effective refractive indices of the two supported slab modes.
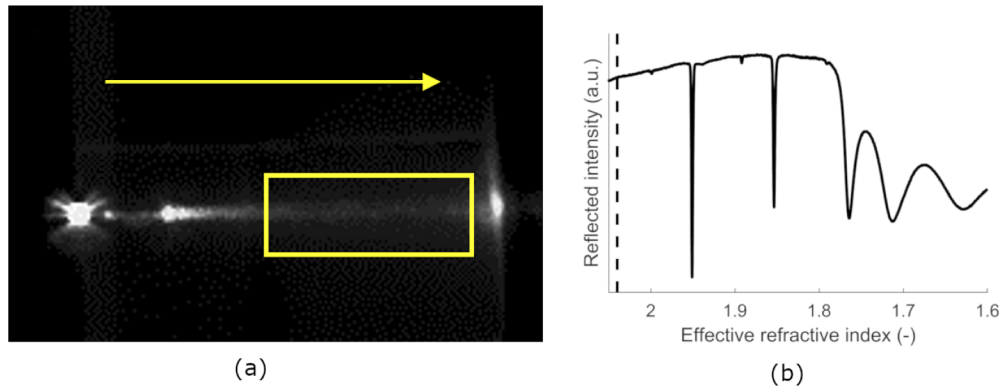
Fig. 10. (a) Top camera image of the scattering loss in a slab waveguide produced by 9 MeV carbon ion irradiation and subsequent annealing at 350°C, at a wavelength of 1550 nm. The arrow indicates direction of propagation and the square the area used to measure the scattering loss. (b) The reflected intensity in a prism coupling setup (Metricon 2010/M) as function of propagation constant, indicating the existence of two modes at a wavelength of 1550 nm. Radiating modes are visible at propagation constants below 1.8.

4.   Discussion

The Raman line scans shown in Fig. 2–3 indicate damage to the $KY(WO_4)_2$ crystalline structure as a result of the 12 MeV carbon ion irradiation, evidenced by the peak broadening and the decrease in peak intensity. The decrease of the Raman yield and the appearance of a broad band profile at 953 cm^{-1} for high ion fluences indicate structural amorphization. The structural damage profiles as function of depth, and especially the locations of the minimum Raman yield, are in good agreement with the electronic and nuclear stopping force profiles calculated using SRIM-2013, and indicate the dominance of electronic damage, as expected from the results of previous research [24]. An inversely proportional relation between the intensity of the $KY(WO_4)_2$ characteristic Raman peaks and the ion fluence is apparent from Fig. 3 for regions where the damage is below the amorphization threshold, caused by the increasing overlap of the amorphous tracks created along the ion trajectories [38]. Figure 3 also shows a shift of the maximum of the nuclear damage deeper into the material for increasing ion fluence. The lower material density of the damaged $KY(WO_4)_2$ lowers the energy loss per unit length of the ions, allowing them to penetrate deeper into the material. This shifts the maximum of the nuclear stopping force, as well as the maximum of the electronic stopping force deeper into the substrate. Additionally, the shift of the vibrational frequency indicates strain in the material, and previous work on the similar $PbWO_4$ indicates that a shift to a lower frequency is due to tensile strain [39].

Both Raman and HRXRD are in good agreement on the location of the electronic and nuclear damage maxima, which both can be seen as having a different effect on the material: below the amorphization threshold, the main effect of the electronic damage is strain induction while the nuclear interactions cause significant point defects and hence disorder in the material. The decrease in Raman yield can be explained by a combination of point defects (disordered background), grain formation (loss of polarization-dependent Raman signal) and broadening due to strain. The strain measured by HRXRD indicates an increase in the lattice parameter (which in turn causes a decrease of refractive index) in agreement with the indication of tensile strain by shift of the Raman frequency. For increasing ion fluence the accumulated damage in the electronic region also significantly damages the crystal structure. This starts with the formation of polycrystalline grains (Fig. 5(b)) but finally causes full amorphization (Fig. 5(c)).

The DWF indicates an imperfect structure, such as amorphous, polycrystalline etc. The presence of strain allows us to determinate the nature of the deformations. In our case, the deformed layer is polycrystalline. This can be seen in the TEM images (Fig. 4), where the crystallite size at increasing depth decreases to a "practically amorphous state". At the same time, the deformation profile indicates that, both at a depth of 2.5 μm and in the region of ion deposition, the lattice deformation is 0.6%-0.78%. Therefore, the obtained values of DW factors should be associated with an increase in the dispersion of polycrystalline grains.

Annealing of the irradiated samples at several temperatures shows a consistent effect on the structure that depends on the damage caused in the material by the irradiation. Below the amorphization threshold, i.e., for fluences $<2.7 \cdot 10^{14}$ ions/cm^2 shown in Fig. 6(a), increasing the annealing temperature results in a steady repair of the KY(WO$_4$)$_2$ crystalline structure, both the electronic and nuclear damage. For these fluences, there is no broadband Raman peak visible at 953 cm^{-1}, which means that the increase in the 906 cm^{-1} peak intensity is caused by consolidation of the vibrational bond causing this peak. Nuclear damage repair as well as strain relieve and partial recrystallization in the defect accumulation region are visible in the HRXRD after annealing (Fig. 7). This combination indicates a further breakdown of the single crystalline structure. The repaired polycrystalline material has a lower amount of strain (0.2% vs. 0.6% in Fig. 4(b)) because annealing allows the crystalline structure to resettle, while the DW factor partially restores due to recombination of displaced atoms and vacancies and the ordering of the crystallites. Annealing at higher temperatures is under test as it might further repair the crystalline structure, although some damage in the material will be permanent, and high-temperature annealing is limited to the transition temperature of α-KY(WO$_4$)$_2$ around 1010°C [40]. For the higher fluences shown in Fig. 6–7, the irradiation-induced damage is permanent and the slight increase in intensity of the 953 cm^{-1} Raman peak indicates consolidation of the amorphous phase. The 0-2 μm region in Fig. 6(b) indicates a slight repair of the crystalline structure after annealing at 350°C. The depth profile of the 953 cm^{-1} peak at this temperature in Fig. 6(c) indeed shows a narrowing of the damage barrier and also indicates that the below-amorphization damage is still repaired, creating a more step-like damage profile, although this is not certain because the changes are close to the limit in the resolution of the microscope utilized.

5.   Summary and conclusions

The high Raman-activity of KY(WO$_4$)$_2$ and other potassium double tungstates allows for the detection of small changes in the vibrational properties caused by irradiation with 12 MeV carbon ions. In this work, both qualitative and quantitative analysis of the structural effects of carbon ion irradiation in KY(WO$_4$)$_2$ have been performed using confocal Raman microscopy, HRXRD and TEM for several ion fluences and subsequent annealing of the samples. The results show a gradual damage profile as function of depth that is in good agreement with SRIM-2013 simulations, and a direct relation between the amount of damage and the ion fluence up to full amorphization. The regions above and below amorphization threshold show a different response to subsequent annealing steps at temperatures between 200-350°C; while the original crystalline structure is partially repaired in regions with partial damage, the fully amorphized regions show an even further destruction of the crystalline structure for increasing temperatures. This effect could be exploited to fabricate samples with a more step-like damage profile by tuning of the ion fluence and annealing process.

The Raman and HRXRD measurements show that it is possible to use swift ion irradiation as a method to fabricate a barrier in KY(WO$_4$)$_2$ with material properties different from unirradiated KY(WO$_4$)$_2$. The micro-reflectivity measurements show that these structural changes induce a refractive index profile as a function of depth, creating planar waveguides in KY(WO$_4$)$_2$. The ion fluence can be used to tune the extent of the damage, which in turn determines the refractive index change. A subsequent annealing step repairs non-permanent damage according to Raman

and HRXRD measurements, and decreases the scattering losses. It should be noted that the irradiation will cause some permanent damage close to the crystal surface. As a consequence, higher ion fluences will increase scattering losses, even after annealing at a high temperature. Samples irradiated with ion fluences showing regions with full amorphization (e.g., fluences >2.7•10^{14} ions/cm^2) show potential for fabricating optical waveguides with a close to step-like refractive index profile, provided that the transmission losses can be kept to acceptable levels.

A slab waveguide fabricated with 9 MeV carbon ions with a fluence of 2.7•10^{14} ions/cm^2 was shown to exhibit two modes. A propagation loss of ~1.5 dB/cm was characterized for the fundamental mode.

Funding

Acknowledgements

Disclosures

The authors declare no conflicts of interest.

References

1. C. Grivas, "Optically pumped planar waveguide lasers: Part II: Gain media, laser systems, and applications," Prog. Quantum Electron. **45-46**, 3–160 (2016).
2. Z. Zhou, B. Yin, and J. Michel, "On-chip light sources for silicon photonics," Light: Sci. Appl. **4**(11), e358 (2015).
3. K. Yamada, T. Tsuchizawa, H. Nishi, R. Kou, T. Hiraki, K. Takeda, H. Fukuda, Y. Ishikawa, K. Wada, and T. Yamamoto, "High-performance silicon photonics technology for telecommunications applications," Sci. Technol. Adv. Mater. **15**(2), 024603 (2014).
4. J. Pfeifle, V. Brasch, M. Lauermann, Y. Yu, D. Wegner, T. Herr, K. Hartinger, P. Schindler, J. Li, D. Hillerkuss, R. Schmogrow, C. Weimann, R. Holzwarth, W. Freude, J. Leuthold, T. J. Kippenberg, and C. Koos, "Coherent terabit communications with microresonator Kerr frequency combs," Nat. Photonics **8**(5), 375–380 (2014).
5. P. Ma, D. Y. Choi, Y. Yu, X. Gai, Z. Yang, S. Debbarma, S. Madden, and B. Luther-Davies, "Low-loss chalcogenide waveguides for biosensing in the mid-infrared," in *Proceedings - 2014 Summer Topicals Meeting Series, SUM 2014*, (IEEE, 2014), pp. 59–60.
6. N. M. Pires, T. Dong, U. Hanke, and N. Hoivik, "Recent developments in optical detection technologies in lab-on-a-chip devices for biosensing applications," Sensors **14**(8), 15458–15479 (2014).
7. C. V. Poulton, A. Yaacobi, D. B. Cole, M. J. Byrd, M. Raval, D. Vermeulen, and M. R. Watts, "Coherent solid-state LIDAR with silicon photonic optical phased arrays," Opt. Lett. **42**(20), 4091 (2017).
8. A. A. Kovalyov, V. V. Preobrazhenskii, M. A. Putyato, O. P. Pchelyakov, N. N. Rubtsova, B. R. Semyagin, V. E. Kisel', S. V. Kuril'chik, and N. V. Kuleshov, "115 fs pulses from Yb^{3+}:KY(WO$_4$)$_2$ laser with low loss nanostructured saturable absorber," Laser Phys. Lett. **8**(6), 431–435 (2011).
9. U. Griebner, S. Rivier, V. Petrov, M. Zorn, G. Erbert, M. Weyers, X. Mateos, M. Aguiló, J. Massons, and F. Díaz, "Passively mode-locked Yb:KLu(WO$_4$)$_2$ oscillators," Opt. Express **13**(9), 3465 (2005).
10. A. A. Lagatsky, F. Fusari, S. Calvez, J. a. Gupta, V. E. Kisel, N. V. Kuleshov, C. T. a. Brown, M. D. Dawson, and W. Sibbett, "Passive mode locking of a Tm,Ho:KY(WO$_4$)$_2$ laser around 2 microm," Opt. Lett. **34**(17), 2587–2589 (2009).
11. A. Beyertt, D. Nickel, and A. Giesen, "Femtosecond thin-disk Yb:KYW regenerative amplifier," Appl. Phys. B: Lasers Opt. **80**(6), 655–660 (2005).
12. F. Brunner, G. J. Spühler, J. Aus der Au, L. Krainer, F. Morier-Genoud, R. Paschotta, N. Lichtenstein, S. Weiss, C. Harder, A. A. Lagatsky, A. Abdolvand, N. V. Kuleshov, and U. Keller, "Diode-pumped femtosecond Yb:KGd(WO$_4$)$_2$ laser with 1.1-W average power," Opt. Lett. **25**(15), 1119 (2000).
13. A. A. Kaminskii, P. V. Klevtsov, L. Li, and A. A. Pavlyuk, "Stimulated emission from KY(WO$_4$)$_2$: Nd^{3+} crystal laser," Phys. Stat. Sol. (a) **5**(2), K79–K81 (1971).

14. V. Petrov, M. C. Pujol, X. Mateos, Ò. Silvestre, S. Rivier, M. Aguiló, R. M. Solé, J. Liu, U. Griebner, and F. Díaz, "Growth and properties of KLu(WO$_4$)$_2$, and novel ytterbium and thulium lasers based on this monoclinic crystalline host," Laser Photonics Rev. **1**(2), 179–212 (2007).

15. Z. Cong, Z. Liu, Z. Qin, X. Zhang, H. Zhang, J. Li, H. Yu, and W. Wang, "LD-pumped actively Q-switched Nd:KLu(WO$_4$)$_2$ self-Raman laser at 1185nm," Opt. Laser Technol. **73**, 50–53 (2015).

16. D. Geskus, S. Aravazhi, S. M. García-Blanco, and M. Pollnau, "Giant optical gain in a rare-earth-ion-doped microstructure," Adv. Mater. **24**(10), OP19–OP22 (2012).

17. S. Aravazhi, D. Geskus, K. Van Dalfsen, S. A. Vázquez-Córdova, C. Grivas, U. Griebner, S. M. García-Blanco, and M. Pollnau, "Engineering lattice matching, doping level, and optical properties of KY(WO$_4$)$_2$:Gd, Lu, Yb layers for a cladding-side-pumped channel waveguide laser," Appl. Phys. B: Lasers Opt. **111**(3), 433–446 (2013).

18. K. van Dalfsen, S. Aravazhi, C. Grivas, S. M. García-Blanco, and M. Pollnau, "Thulium channel waveguide laser with 1.6 W of output power and ~80% slope efficiency," Opt. Lett. **39**(15), 4380 (2014).

19. Y.-S. Yong, S. Aravazhi, S. A. Vázquez-Córdova, J. L. Herek, S. M. García-Blanco, and M. Pollnau, "Gain dynamics in a highly ytterbium-doped potassium double tungstate epitaxial layer," J. Opt. Soc. Am. B **35**(9), 2176 (2018).

20. M. A. Sefunc, F. B. Segerink, and S. M. García-Blanco, "High index contrast passive potassium double tungstate waveguides," Opt. Mater. Express **8**(3), 629 (2018).

21. C. I. van Emmerik, S. M. Martinussen, J. Mu, M. Dijkstra, R. Kooijman, and S. M. García-Blanco, "A novel polishing stop for accurate integration of potassium yttrium double tungstate on a silicon dioxide," Proc. SPIE **10535**, 105350U (2018).

22. C. A. Merchant, J. S. Aitchison, S. Garcia-Blanco, C. Hnatovsky, R. S. Taylor, F. Agulló-Rueda, A. J. Kellock, and J. E. E. Baglin, "Direct observation of waveguide formation in KGd(WO$_4$)$_2$ by low dose H$^+$ ion implantation," Appl. Phys. Lett. **89**(11), 111116 (2006).

23. C. A. Merchant, P. Scrutton, C. Hnatovsky, R. S. Taylor, G. García, J. Olivares, A. S. Helmy, S. Member, and J. S. Aitchison, "High-Resolution Refractive Index and Micro-Raman Spectroscopy of Planar Waveguides in KGd(WO$_4$)$_2$ Formed by Swift Heavy Ion Irradiation," IEEE J. Quantum Electron. **45**(4), 373–379 (2009).

24. A. García-Navarro, J. Olivares, G. García, F. Agulló-López, S. García-Blanco, C. Merchant, and J. S. Aitchison, "Fabrication of optical waveguides in KGW by swift heavy ion beam irradiation," Nucl. Instrum. Methods Phys. Res., Sect. B **249**(1-2), 177–180 (2006).

25. M. Pollnau, Y. E. Romanyuk, F. Gardillou, C. N. Borca, U. Griebner, S. Rivier, and V. Petrov, "Double tungstate lasers: from bulk toward on-chip integrated waveguide devices," IEEE J. Sel. Top. Quantum Electron. **13**(3), 661–671 (2007).

26. R. Frentrop, V. Tormo-Márquez, J. Olivares, and S. García-Blanco, "High-contrast slab waveguide fabrication in KY(WO$_4$)$_2$ by swift heavy ion irradiation," Proc. SPIE **10535**, 105350O (2018).

27. X. Mateos, R. Solé, J. Gavaldà, M. Aguiló, J. Massons, and F. Díaz, "Crystal growth, optical and spectroscopic characterisation of monoclinic KY(WO4)2 co-doped with Er3+ and Yb3+," Opt. Mater. **28**(4), 423–431 (2006).

28. A. Climent-Font, F. Pászti, G. García, M. T. Fernández-Jiménez, and F. Agulló, "First measurements with the Madrid 5 MV tandem accelerator," Nucl. Instrum. Methods Phys. Res., Sect. B **219-220**, 400–404 (2004).

29. J. Olivares, G. García, F. Agulló-López, F. Agulló-Rueda, A. Kling, and J. C. Soares, "Generation of amorphous surface layers in LiNbO$_3$ by ion-beam irradiation: Thresholding and boundary propagation," Appl. Phys. A: Mater. Sci. Process. **81**(7), 1465–1469 (2005).

30. J. Lindhard, M. Scharff, and H. Schiott, "Range concepts and heavy ion ranges," Mat. Fys. Medd. Dan. Vid. Selsk. **33**, 1 (1963).

31. J. F. Ziegler, M. D. Ziegler, and J. P. Biersack, "SRIM - The stopping and range of ions in matter (2010)," Nucl. Instrum. Methods Phys. Res., Sect. B **268**(11-12), 1818–1823 (2010).

32. M. A. Krivoglaz, *X-ray and Neutron Diffraction in Non-Ideal Crystals* (Springer, 1996).

33. E. Kreyszig, *Advanced Engineering Mathematics* (John Wiley & Sons, 2010).

34. C. R. Wie, T. A. Tombrello, and T. Vreeland, "Dynamical X-ray diffraction from nonuniform crystalline films: Application to X-ray rocking curve analysis," J. Appl. Phys. **59**(11), 3743–3746 (1986).

35. K. D. Chtcherbatchev, V. T. Bublik, A. S. Markevich, V. N. Mordkovich, E. Alves, N. P. Barradas, and A. D. Sequeira, "The influence of *in situ* photoexcitation on a defect structure generation in Ar$^+$ implanted GaAs(001) crystals revealed by high-resolution X-ray diffraction and Rutherford backscattering spectroscopy," J. Phys. D: Appl. Phys. **36**(10A), A143–A147 (2003).

36. J. Mayer, L. A. Giannuzzi, T. Kamino, and J. Michael, "TEM Sample Preparation and FIB-Induced Damage," MRS Bull. **32**(5), 400–407 (2007).

37. S. G. Blanco, J. S. Aitchison, C. Hnatovsky, and R. S. Taylor, "Microreflectivity characterization of the two-dimensional refractive index distribution of electron-beam-written optical waveguides in germanium-doped flame-hydrolysis silica," Appl. Phys. Lett. **85**(8), 1314–1316 (2004).

38. N. Itoh, D. M. Duffy, S. Khakshouri, and A. M. Stoneham, "Making tracks: electronic excitation roles in forming swift heavy ion tracks," J. Phys.: Condens. Matter **21**(47), 474205 (2009).

39. W. L. Zhu, K. S. Wan, Y. L. Huang, X. Q. Feng, and G. Pezzotti, "Stress dependence of Raman vibrational bands of PbWO$_4$ single crystals," Phys. Stat. Sol. (a) **203**(10), 2376–2385 (2006).

40. A. A. Kaminskii, A. F. Konstantinova, V. P. Orekhova, A. V. Butashin, R. F. Klevtsova, and A. A. Pavlyuk, "Optical and nonlinear laser properties of the $\chi^{(3)}$-active monoclinic α-KY(WO$_4$)$_2$ crystals," Crystallogr. Rep. **46**(4), 665–672 (2001).